JGR Oceans

RESEARCH ARTICLE
10.1029/2024JC022075

Special Collection:
The Arctic Ocean's changing Beaufort Gyre

Key Points:

- Interannual evolution of seasonal sea-ice volume (SIV) changes in the Canada Basin is set primarily by changing thermodynamic processes
- Interannual increases in the amount of wintertime growth are consistent with September SIV declining more rapidly than May SIV
- Seasonal changes in upper ocean heat content can account for about one-third of the atmospheric heat input that is not used to change SIV

Supporting Information:

Supporting Information may be found in the online version of this article.

Correspondence to:
E. Bailey,
elizabeth.bailey@yale.edu

Citation:
Bailey, E., & Timmermans, M.-L. (2025). Investigating the relative roles of dynamics and thermodynamics in sea-ice volume changes in the Canada basin. *Journal of Geophysical Research: Oceans*, *130*, e2024JC022075. https://doi.org/10.1029/2024JC022075

Received 4 NOV 2024
Accepted 13 FEB 2025

Author Contributions:
Conceptualization: Elizabeth Bailey, Mary-Louise Timmermans
Formal analysis: Elizabeth Bailey
Funding acquisition: Mary-Louise Timmermans
Investigation: Elizabeth Bailey
Methodology: Elizabeth Bailey, Mary-Louise Timmermans
Resources: Elizabeth Bailey, Mary-Louise Timmermans
Software: Elizabeth Bailey
Supervision: Mary-Louise Timmermans
Validation: Elizabeth Bailey, Mary-Louise Timmermans
Visualization: Elizabeth Bailey

Investigating the Relative Roles of Dynamics and Thermodynamics in Sea-Ice Volume Changes in the Canada Basin

Elizabeth Bailey[1] and **Mary-Louise Timmermans**[1]

[1]Department of Earth and Planetary Sciences, Yale University, New Haven, CT, USA

Abstract The Canada Basin (CB) has seen significant sea-ice loss in recent decades. We use output from the Pan-Arctic Ice-Ocean Modeling and Assimilation System to examine the 1979–2023 evolution of seasonal sea-ice volume (SIV) changes in the CB partitioned into advective and thermodynamic changes. In winter, some years show net convergence into the region that is of comparable magnitude to the SIV change attributed to sea-ice growth. In summer, melt/ablation dominates the change each year. In both seasons, 44 year trends in seasonal SIV changes are driven primarily by thermodynamic processes. The inferred thermodynamic growth each year is nearly equal to the inferred melt consistent with SIV at the end of the melt season declining more rapidly than SIV at the end of the growth season. Increased melt season atmospheric heating of the ice-ocean system over 1979–2023, estimated from ERA5 reanalysis, is consistent with the ice-albedo feedback. In the growth season, net cumulative atmospheric heat release from the ice-ocean system shows no trend, suggesting increases in inferred thermodynamic ice growth can be attributed to more rapid growth of thinner ice. In each season, cumulative atmospheric heat input exceeds that required for ice melt/growth resulting in a residual that influences ocean heat content (OHC). Seasonal OHC changes, inferred from ocean observations, are equal to approximately one-third of this residual, although limited ocean observations leave the total heat budget poorly constrained, highlighting a need for more water column observations.

Plain Language Summary The Canada Basin (CB) has experienced significant sea-ice loss in recent decades. We examined sea-ice volume (SIV) seasonal changes from 1979 to 2023, dividing these changes into those from ice moving into/out of the CB region and those caused by ice melt/growth. The 44 year trend in SIV changes in each of the summer and winter seasons is due to ice growth/melt in the region, while there are no trends in SIV moving into/out of the region. Sea-ice growth each winter is nearly equal to the volume of sea-ice melt each summer. In winter, the total heat loss has not changed over the 44 years, suggesting more ice growth in recent years because thinner ice requires less cooling to grow the same amount as thicker ice. Each season, there is more than enough heat addition/loss from the atmosphere to melt/grow ice, resulting in leftover heat that influences heat in the ocean. Changes in ocean heat account for approximately one-third of this leftover heat, though limited measurements prevent us from fully accounting for all heat in the region, highlighting the need for more ocean observations.

1. Introduction

From the beginning of the observational record in the late 1970s through the mid-1990s, the Canada Basin (CB) was characterized as a region with a significant amount of old thick ice (J. Maslanik et al., 2011); ice was corralled and stored by the anticyclonic Beaufort High and wind-driven oceanic Beaufort Gyre (Thorndike & Colony, 1982). Sea-ice volume has been declining Arctic-wide with old thick ice being replaced by predominantly seasonal sea ice that does not survive a single melt season (Kwok, 2018). This transition to generally thinner ice, which began around 1998, has been attributed to various factors including anomalous atmospheric forcing (Hutchings & Rigor, 2012; J. A. Maslanik et al., 1999) and an efficient ice-albedo feedback (Perovich, Nghiem, et al., 2007). Despite Arctic-wide ice loss, the CB continues to receive multiyear sea ice (MYI) from the central Arctic driven by the large-scale anticyclonic circulation (D. Babb et al., 2020; G. Moore et al., 2022; D. G. Babb et al., 2022). However, thinner ice has been entering the basin in recent years and less MYI survives through summer in the CB (D. G. Babb et al., 2022).

Sea-ice thinning and upper ocean heat content (OHC) in the CB are influenced significantly by the accumulation of solar heat during summer. This heat can be trapped below a seasonal mixed layer, formed by relatively fresh

Writing – original draft: Elizabeth Bailey, Mary-Louise Timmermans
Writing – review & editing: Elizabeth Bailey, Mary-Louise Timmermans

sea-ice meltwater, in a near surface temperature maximum (NSTM) layer (Jackson et al., 2010; Timmermans, 2015). The heat in the NSTM can dissipate during fall and winter through convective or mechanical mixing, which can influence wintertime ice growth (Perovich et al., 2008; Timmermans, 2015). In the CB, Pacific-origin waters also store heat below the mixed layer, although the strong halocline stratification generally prevents significant vertical heat fluxes into the mixed layer (Toole et al., 2010). An effective ice-albedo feedback in the CB and margins, influenced by increased heat transport via Bering Strait (Woodgate et al., 2010), is associated with increased summertime solar heating of the ocean (linear trend of approximately 2–5 W m^{-2} per decade over 1979–2021; Perovich, Light, et al., 2007; Timmermans & Toole, 2023). This has been a primary driver of sea-ice loss in the region, dominated by bottom ablation, with extreme losses in the CB in 1998, 2007, and 2012 (J. A. Maslanik et al., 1999; Perovich et al., 2008; Zhang et al., 2013). Despite significant progress in understanding sea-ice losses in the CB, no studies have fully assessed ice losses in the context of both atmospheric and oceanographic heat budgets.

To elucidate the driving mechanisms behind sea-ice loss in the CB region, we analyze atmospheric and sea-ice volume (SIV) fluxes over the 1979–2023 period as well as oceanographic observations to evaluate the heat budget of the ice-ocean system and its interannual and seasonal evolution in the CB. We partition SIV changes into those arising from net advection into and out of the region and those that result from thermodynamic changes within the region. We consider residual heat in the melt and growth seasons in context with changes in OHC. Our results shed light on important feedback in the system and highlight critical observational gaps.

A brief outline of the paper is as follows. The next section describes the data sets and methods used to evaluate SIV changes, net atmospheric heat input to the CB, and OHC in the region. In Section 3.1, we quantify interannual trends in seasonal SIV changes in the growth and melt seasons and delineate dynamic (ice advection) versus thermodynamic contributions to these trends. In Section 3.2, we evaluate the atmospheric heat fluxes by melt/growth seasons and corresponding trends. In Section 3.3, we quantify residuals in the sea ice and atmospheric heat budgets and set this in context with the ocean heat budget. Section 4 provides a summary and discussion of the results.

2. Data and Methods

2.1. Sea-Ice Volume Budget

Sea-ice volume and ice volume fluxes within and into and out of the CB (Figure 1a) are inferred from the Pan-Arctic Ice-Ocean Modeling and Assimilation System (PIOMAS). Pan-Arctic Ice-Ocean Modeling and Assimilation System is a coupled ocean-sea-ice model that assimilates ice concentration and velocity information; full details are given by (Zhang & Rothrock, 2003). The surface heat budget for PIOMAS is driven by National Centers for Environmental Prediction/National Center for Atmospheric Research (NCEP/NCAR) reanalysis fluxes (see Kalnay et al., 1996; Zhang & Rothrock, 2003). Here, we use daily data with a mean spatial resolution of approximately 30 km. The uncertainty for ice velocities is approximately 8% of the observed in situ ice drift (Zhang & Rothrock, 2003). The uncertainties associated with sea-ice concentration (SIC) are $\leq 5\%$ given estimates from the data products assimilated by PIOMAS (Brucker et al., 2014).

Upward-looking sonar (ULS) data from the Beaufort Gyre Observing System (BGOS) moorings, at the locations shown in Figure 1a, provide in situ ice draft measurements, which allow for inferences of sea-ice thickness that can be used to evaluate PIOMAS in the CB (Figure 1b; R. A. Krishfield et al., 2014). Details of the measurement and processing are given by R. A. Krishfield et al. (2014). A conversion factor of 1.123 is used to convert ice draft to thickness with estimates accurate to ±10 cm (Melling et al., 1995; R. A. Krishfield et al., 2014). Compared to the in situ ULS observations, the modeled ice thickness from PIOMAS reasonably captures observed ice thickness ($r = 0.81$; Figure 1b and Figure S1a in Supporting Information S1). Schweiger et al. (2011) deduced a mean thickness uncertainty of 0.17 m for PIOMAS, which equates to a value for SIV uncertainty of about 1.73×10^8 km^3 for the CB. In addition, the thickness of thin ice is typically overestimated and the thickness of thick ice is underestimated (Figure S1b in Supporting Information S1), which is evident when comparing the mean seasonal cycle of sea-ice thickness between PIOMAS and ULS observations (Figure 1b; Schweiger et al., 2011; X. Wang et al., 2016). The very thick floes may not be well produced in PIOMAS because the dynamical process of ice ridging relies on parameterization.

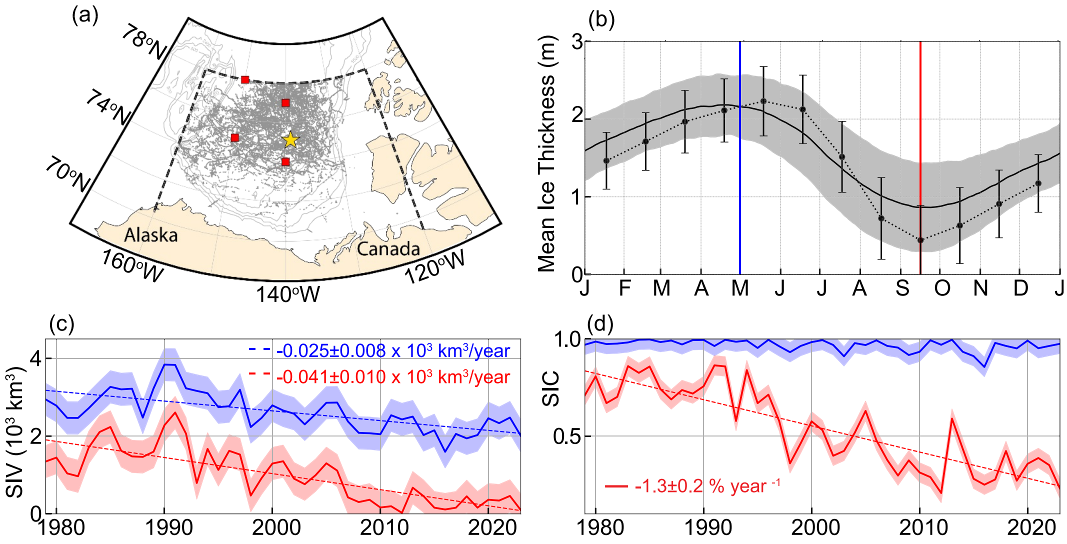

Figure 1. (a) A map of the Canada Basin (CB) region bounded by 78°N and the Canadian-Alaskan Coastline as well as 160°W and 120°W following Rheinlænder et al. (2024). The yellow star is the location of upper ocean profiles in Figure 2 with all available ocean observations shown in gray and the location of the Beaufort Gyre Observing System (BGOS) moorings at the red squares, (b) The mean seasonal cycle of daily ice thickness from Pan-Arctic Ice-Ocean Modeling and Assimilation System (PIOMAS) (solid) for the CB from 1979 through 2023 with one standard deviation shaded, and monthly mean ice thickness from BGOS Upward-looking sonar (dotted) from 2003 to 2023. An ice draft to ice thickness conversion factor of 1.123 is used following R. A. Krishfield et al. (2014). Vertical lines indicate May 1 (blue) and September 15 (red) corresponding to the beginning and end of the defined seasons. A timeseries of (c) sea-ice volume and (d) mean sea-ice concentration (SIC) from PIOMAS on May 1 (blue) and September 15 (red) for the CB from 1979 to 2023. Uncertainties are shaded based on Schweiger et al. (2011). Significant linear trends are given with 95% confidence intervals. There are no statistically significant trends for May 1 SIC.

The seasonal cycle of sea-ice thickness from PIOMAS for the period of record (1979–2023) has the thickest ice around May 1 of each year and the thinnest around September 15 (Figure 1b). Hence, we define the melt season from May 1 to September 15 and the growth season from September 15 to May 1 of the following year (Figure 1b). We refer to May 1 to September 15 as the "Melt Season", where this terminology is taken to encompass all processes that lead to reduced sea-ice cover in the region (e.g., surface melt, under-ice ablation, and sea-ice divergence). Similarly, the period from September 15 to May 1 of the following year is termed the "Growth Season." This terminology is used to broadly encompass all processes that give rise to a larger volume of sea ice in the region (e.g., thermodynamic growth and sea-ice convergence).

We introduce the total volume change over the course of either a melt or growth season: $\Delta V_{To} = V_f - V_i$, where V_f and V_i are the final and initial SIV, respectively, in the CB. A negative (positive) SIV change corresponds with a net decrease (increase) in SIV in the CB. Then, volume changes due to local thermodynamics can be inferred as $\Delta V_{Th} = \Delta V_{To} - \Delta V_U$, where ΔV_U is the total SIV change in the CB that results from advection and ΔV_{Th} is the inferred SIV change due to local thermodynamics (growth, surface melt or bottom ablation, where $\Delta V_{Th} > 0$ implies net growth). The advective component, ΔV_U, is the sum of the SIV fluxed across the northern, eastern, and western CB boundaries (i.e., $\Delta V_U = \Delta V_U^N + \Delta V_U^E + \Delta V_U^W$ and $\Delta V_U > 0$ implies net transport into the CB). The volume fluxed across each boundary for any given season is calculated as

$$\Delta V_U = \sum_{t=0}^{m} \sum_{k=0}^{n} SIC_{kt} h_{i,kt} u_{i,kt} l_{kt}, \tag{1}$$

where k is each grid cell along a boundary, n is the number of grid cells along the boundary, h_i is the sea-ice thickness, u_i is the sea-ice velocity normal to the boundary, l is the distance between points along the boundary, t is the timestep (daily), and m is the number of days in either season. Velocity components were rotated such that the x and y components were aligned with lines of longitude and latitude, respectively, and interpolated onto the line of latitude/longitude for each boundary before flux calculations. Throughout this paper, we convert SIV to equivalent heat units (i.e., Joules) by multiplying SIV by sea-ice density (ρ_i; taken as 900×10^9 kg km^{-3}) and the latent heat of freezing (L_f; taken to be 2.67×10^5 J kg^{-1}). This choice is made so that each component of the atmosphere-ice-ocean heat budget can be compared directly.

2.2. Atmospheric Fluxes

To assess the atmospheric component of the heat budget, we have chosen to use the ERA5 reanalysis provided by the European Centre for Medium-Range Weather Forecasts (ECMWF) (Hersbach et al., 2018) as it has been found to have the smallest biases from Arctic observations compared to other products (Graham et al., 2019). Furthermore, the ERA5 components of the surface energy budget are well-correlated with the NCEP/NCAR components used in PIOMAS (Graham et al., 2019; Seo et al., 2020). A comparison of the ERA5 and NCEP/NCAR reanalysis radiative components of the surface energy budget is given by Seo et al. (2020), who found them to be well correlated ($r = 0.99$). Both ERA5 and NCEP/NCAR fluxes also have similar biases when compared to in situ observations (see Table 1 of Graham et al., 2019).

The net atmospheric heat input into the surface ice-ocean system for any given season is calculated as $Q_{a,net} = Q_{ai,net} + Q_{ao,net}$, where $Q_{ai,net}$ is the net cumulative atmospheric heat input into the sea-ice surface and $Q_{ao,net}$ is the net cumulative atmospheric heat input into the ocean surface. Atmospheric heat input into the sea-ice surface is calculated as

$$Q_{ai} = SIC[(1 - \alpha_i)\, Q_{SW} + Q_{LW} + Q_s + Q_\ell], \tag{2}$$

where SIC, incoming shortwave radiation (Q_{SW}), longwave radiation (Q_{LW}), sensible heat (Q_s), and latent heat (Q_ℓ) fluxes (positive downwards) were taken from the ERA5 hourly reanalysis product. We note SIC is well-correlated between PIOMAS and ERA5 ($r = 0.99$; Figure S1c in Supporting Information S1). The largest differences occur at low SICs, where the mean difference between PIOMAS and ERA5 for SIC less than 0.5 is approximately 0.08 (standard deviation of 0.04). The albedo of sea ice, α_i, is taken to be 0.7. This choice is a simplification of sea-ice albedo, which has been shown to vary between 0.9 and 0.2 seasonally (Perovich & Polashenski, 2012). Further discussion of the influence of this choice on our results is given in Section 4. Similarly, the atmosphere-ocean heat input is

$$Q_{ao} = (1 - SIC)[(1 - \alpha_w)\, Q_{SW} + Q_{LW} + Q_s + Q_\ell], \tag{3}$$

where α_w is the albedo of seawater taken to be 0.07 (Pegau & Paulson, 2001). The ERA5 data product has a horizontal resolution of $0.25° \times 0.25°$. For each season, the cumulative atmospheric heat input into the surface ice-ocean system $(Q_{a,net})$ was calculated by taking the cumulative sum of Q_{ai} and Q_{ao} over each ERA5 grid cell within the CB (Figure 1) over the course of the season in question.

Many studies have evaluated uncertainties associated with ERA5 reanalysis for the Arctic region compared to observations as well as other reanalysis products (e.g., Batrak & Müller, 2019; Graham et al., 2019; C. Wang et al., 2019; Renfrew et al., 2021; Herrmannsdörfer et al., 2023). Here, we use the bias estimates of Graham et al. (2019) for ERA5 fluxes (see Table S1 in Supporting Information S1) to estimate uncertainty in each of the terms in Equations 2 and 3 as well as the 0.06 uncertainty estimate for ERA5 SIC from Renfrew et al. (2021). For this estimation, the sum of the fractional uncertainties (i.e., the cumulative biases derived from Table S1 in Supporting Information S1 over the cumulative flux value from ERA5 throughout a given season) of each term in Equations 2 and 3 is taken as the overall uncertainty for the net cumulative atmospheric flux for either season. We further note that Renfrew et al. (2021) found that near-surface fluxes are well represented in ice-free conditions, whereas conditions with partial ice coverage have two to three times larger uncertainty. We do not explicitly account for these differences in our uncertainty treatment.

2.3. Oceanographic Setting and Observations

Ice-Tethered Profilers (ITPs) provide year-round water-column measurements of temperature and salinity between 7 and 750 m depth (R. Krishfield et al., 2008; Toole et al., 2011); ITP system and processing procedures are documented by R. Krishfield et al. (2008). In addition to ITP observations, ship-based conductivity, temperature, and depth (CTD) data from the annual BGOS/Joint Ocean Ice Study (JOIS) expeditions (limited to summer/fall

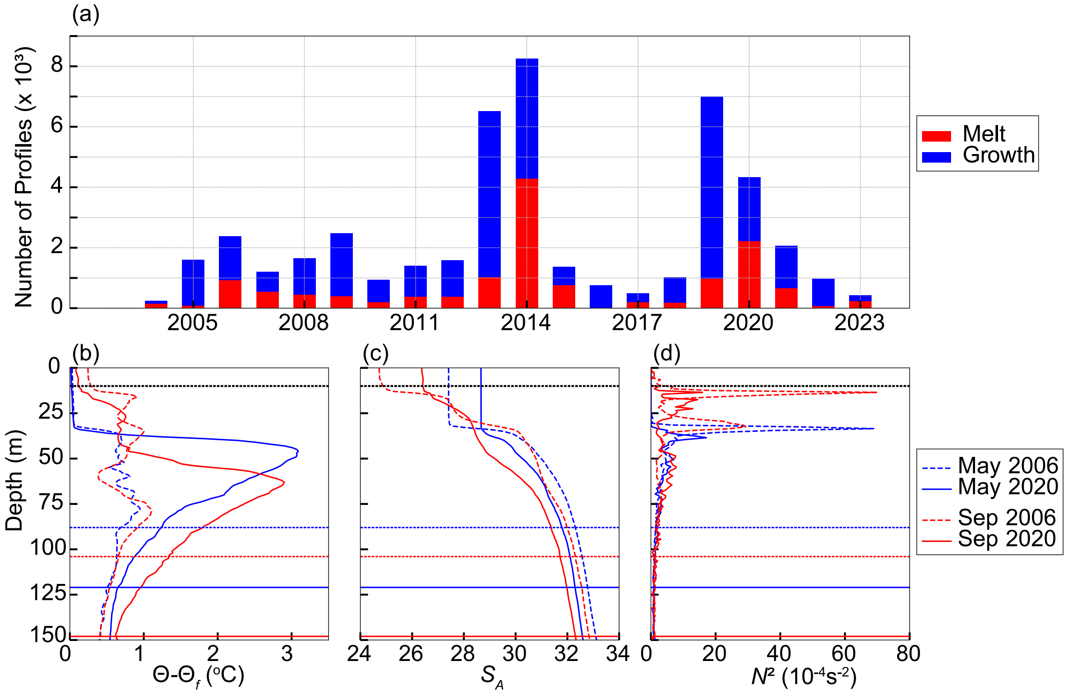

Figure 2. (a) Number of analyzed ocean profiles of temperature and salinity in the melt (red) and growth (blue) seasons, for 2003 through 2023 in the Canada Basin region (gray dots, Figure 1a). Profiles of (b) conservative temperature relative to the conservative freezing point temperature $(\Theta - \Theta_f)$, (c) absolute salinity (S_A), and (d) buoyancy frequency (N^2) from May (i.e., the end of the growth season; blue) and September (i.e., end of the melt season; red) near the beginning of the observational record (2006; dashed) and near the end (2020; solid) at the location of the star in Figure 1a. Dashed lines at 10 m and at the depth of $S_A = 32.3$ give an indication of the depth range considered in the *OHC* calculations.

months) were used (Proshutinsky et al., 2019). The number of ITP and CTD profiles (shown as gray dots in Figure 1a) varies year to year from the most profiles in 2014 to the fewest in 2003, though some years have few to no observations when considering any individual season (e.g., the 2016 melt season; Figure 2a). In addition, water column observations have spatial limitations in any given year. Of note is that the continental shelf regions, where much of the significant ocean change occurs, are particularly poorly sampled (Figure 1a). We analyze ocean data spanning 2003–2023 with the start of the record coinciding with the start of the BGOS/JOIS program and the ITP program (i.e., with the former providing spatially comprehensive measurements over the CB each year and the latter providing the first comprehensive year-round measurements in the CB). On the other hand, the sea-ice and reanalysis data analyzed here span 1979–2023 with the start of the record coinciding with the start of the satellite record. For this reason, our heat budget assessments that include the ocean are only done for the latter part of the full record analyzed.

The general structure of the water column is as follows. At the end of the growth season (i.e., May 1, before the onset of sea-ice melt and summertime ocean heating), the surface mixed layer is effectively at the seawater freezing temperature and relatively salty with the base of the mixed layer at approximately 30 m for the CB (Figures 2b and 2c). Below the mixed layer is a subsurface reservoir of heat known as the Pacific Summer Water layer (PSW; Figure 2b). We define the PSW layer to be between 30 m and the depth of the isohaline (in terms of absolute salinity) $S_A = 32.3$ (e.g., Arroyo et al., 2023); the deep bound coincides approximately with the top of the cold Pacific Winter Water layer (Figure 2b). During the melt season, a seasonal mixed layer forms near the surface from cold relatively fresh meltwater (Figures 2b and 2d). The formation of a strongly stratified seasonal mixed layer in summer yields a mixed-layer depth of around 10–15 m (see Peralta-Ferriz & Woodgate, 2015). This seasonal mixed layer often leads to the storage of heat in a NSTM, typically found between 10 and 30 m depth in the CB (Figure 2b), that has been shown to inhibit the growth of ice when it is mixed to the surface (Timmermans, 2015).

In Section 3.3, we explore the OHC over 2003–2023 in context with sea-ice volume and atmospheric heat budgets. Integrated OHC (OHC) in the PSW layer is calculated as

$$OHC = \int_{10}^{d_{S_A=32.3}} \rho_w(z) c_p(z) \left[\Theta(z) - \Theta_f(z)\right] dz, \tag{4}$$

where ρ_w is the seawater density, c_p is the heat capacity, and Θ_f is the conservative freezing temperature; the integral is taken between 10 m and the depth of the $S_A = 32.3$ isohaline. All available ITP and CTD temperature and salinity profiles in the CB from 2003 to 2023 (Figures 1a and 2a) are used in the estimate and a 30 day running mean is computed.

Since ITP profiles are limited to observations deeper than 7 m, we use sea surface temperature (SST) and sea surface salinity (SSS) from ERA5 to account for the heat content in the surface layer of the ocean, which we define from the surface to 10 m and assume to have uniform temperature and salinity properties. The ERA5 reanalysis SST/SSS data have the same spatial resolution (0.25° × 0.25°) and temporal resolution (hourly) as the atmospheric fluxes and SIC described in Section 2.2 (Hersbach et al., 2018). ERA5 SST data have shown good agreement with in situ buoy data in the CB though a cold bias is present ($r = 0.99$ with a root mean square error of 0.36°C; Kong et al., 2022), and SSS values are well correlated (correlation coefficient of 0.6) with in situ measurements in the region (Hall et al., 2021). The SST product includes a temperature constraint that sets SSTs to the local seawater freezing temperature (a function of SSS) when SIC is greater than 0.55 (Mogensen et al., 2012).

Typical CB surface ocean conditions are as follows. From November through May, areal mean SSTs are typically at or near the freezing temperature over the entire region (Figure S2 in Supporting Information S1). The surface layer becomes saltier over the course of the growth season (from September through May) with ice growth, mixing and entrainment of deeper waters, and the shut off of fresh river input. During the melt season, the warmest SSTs occur in August (Figure S2 in Supporting Information S1), though this can vary from mid-July to the beginning of September. The freshest surface waters occur in July and August as ice melt and river runoff provide freshening (Figure S2 in Supporting Information S1). Spatially, the warmest SSTs are in the southeastern region of the CB in the vicinity of the continental shelf since waters at the basin margins where ice retreats earliest in the season receive the longest duration of solar warming (Figures S3–S5 in Supporting Information S1). SSTs tend to remain cool and near freezing temperature in the north and center of the region (Figure S5 in Supporting Information S1). Ocean heat content in the surface layer (shallowest 10 m) is estimated in an analogous manner to Equation 4 on the assumption that SST and SSS are uniform in this layer.

3. Results

3.1. Dynamic and Inferred Thermodynamic Changes in Sea-Ice Volume

Sea-ice volume has been decreasing both at the beginning of May as well as in mid-September (Figure 1c). May 1 SIV is decreasing at a rate of $-2.5 \pm 0.8 \times 10^{10}$ km^3 year^{-1} (Figure 1c). In contrast, there has been no statistically significant trend in May 1 SIC from 1979 to 2023 (Figure 1d). September 15 SIV has been decreasing at a rate of $-4.1 \pm 1.0 \times 10^{10}$ km^3 year^{-1} (Figure 1c). However, recent years have seen a slow in this September SIV decline. September 15 SIC has also declined at approximately 13% ± 2% decade^{-1} (Figure 1d).

Although SIV is becoming smaller at both the beginning (September) and end (May of the following year) of the growth season (Figure 1c), there has been a greater sea-ice volume decrease in September compared to May. This leads to an increase in the change in SIV over the growth season (a linear trend of $3.3 \pm 1.9 \times 10^{18}$ J year^{-1} over the period of record, 1979–2023; Figure 3a). For the same reason, there has been an increase in the change in SIV during the melt season with a linear trend of $-3.4 \pm 1.3 \times 10^{18}$ J year^{-1} (Figure 3b).

In the growth season, ice fluxes across the northern boundary are typically into the CB (positive; Figure 4a, purple). Sea ice generally exits the region across the western boundary (negative fluxes; Figure 4a, orange). Ice speeds are faster across the western boundary than across the northern (Figure S6 in Supporting Information S1) with the overall circulation patterns consistent with the large-scale anticyclonic wind forcing. Still, anomalous fluxes can occur, such as in the growth season of 1997/1998 where southerly and easterly winds increased

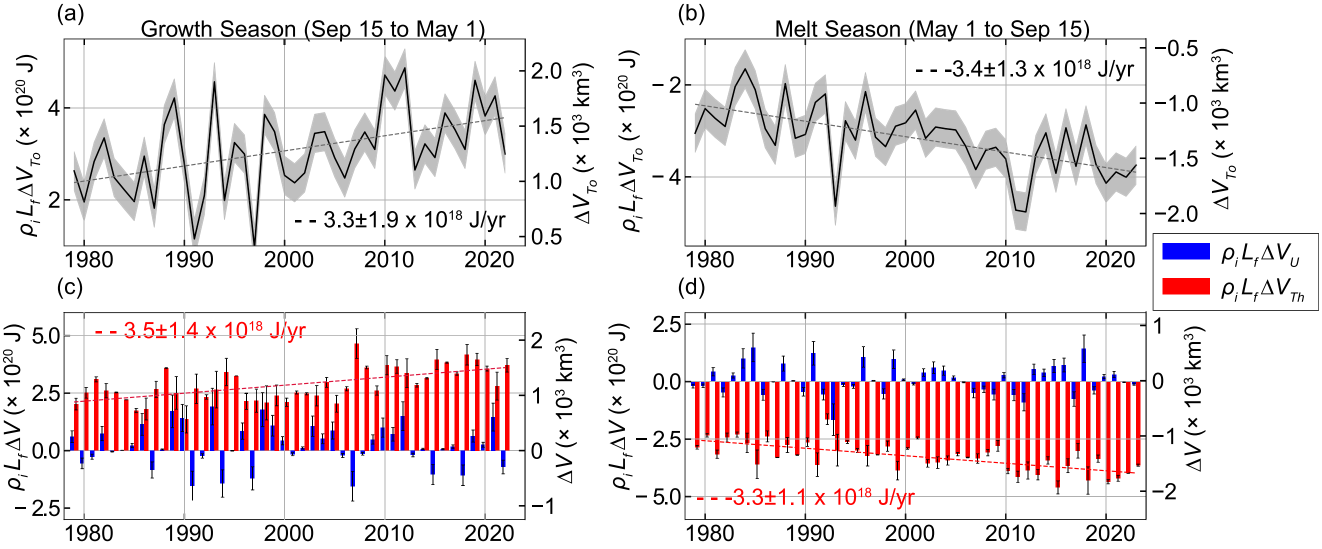

Figure 3. Timeseries of the heat required for the total change in sea-ice volume for the Canada Basin (CB) during the (a) growth season (September 15 to May 1 of the following year) and (b) melt season (May 1 to September 15) for 1979–2023. Shading indicates Pan-Arctic Ice-Ocean Modeling and Assimilation System (PIOMAS) volume uncertainty estimates based on Schweiger et al. (2011). The net cumulative advective (blue) and inferred thermodynamic (red) volume fluxes in terms of heat for the (c) growth season and (d) melt season in the CB. Positive advective flux values indicate a net volume flux into the CB and positive thermodynamic flux values indicate net ice growth in the CB. Shading and error bars indicate volume flux uncertainty estimates based on Schweiger et al. (2011) and Zhang and Rothrock (2003). Linear trends are given with 95% confidence intervals. There are no statistically significant trends in net cumulative advective volume fluxes over the period for either season. Data are from PIOMAS. Year labels for the growth season denote the year in which the season began.

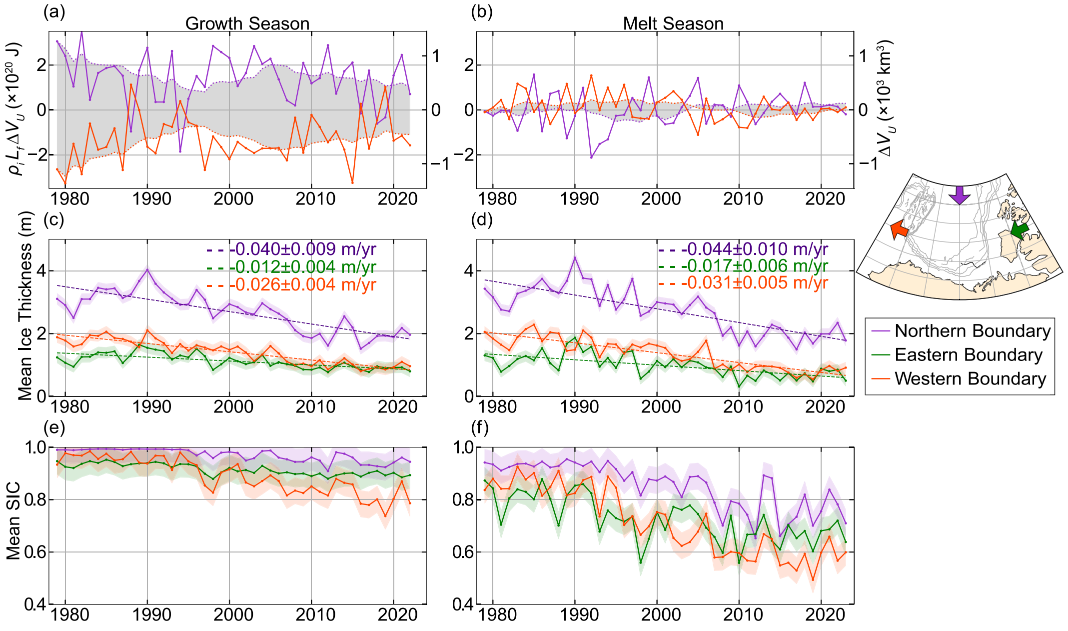

Figure 4. Timeseries of the cumulative ice volume advective flux (in terms of heat) across the northern (purple) and western (orange) boundaries (map inset) for (a) the growth season and (b) the melt season; dotted lines indicate the respective 10 year running means. Positive (negative) values indicate an import into (export out of) the Canada Basin. Timeseries of the mean ice thickness fluxed across each boundary for (c) the growth season and (d) the melt season, and mean sea-ice concentration for (e) the growth and (f) melt seasons. Shading indicates ice thickness uncertainty estimates based on Schweiger et al. (2011) and ice concentration uncertainties based on the assimilated products. Linear trends over the period with 95% confidence intervals are shown for panels (c) and (d). The growth season is labeled with the year in which the season began.

(decreased) the export (import) of ice across the western (northern) boundary (J. A. Maslanik et al., 1999), leading to year-to-year variability of net ice convergence (Figures 3c and 4a). Further, we note that periods of anomalous transport within any given season can be masked by this seasonal mean (e.g., the enhanced western boundary export associated with the winter 2013 breakup event, see Rheinlænder et al. (2024)). Overall, SIV fluxes into and out of the CB in the growth season are decreasing (Figure 4a), which can be attributed to reduced ice thickness and concentration (Figures 4c and 4e). This is in agreement with Howell et al. (2016), who noted reduced sea-ice area fluxes across the western boundary from 2008 to 2014. By contrast, there is no statistically significant trend in ice speeds over 1979–2023 (Figure S6 in Supporting Information S1). We do note that over shorter periods, trends to faster drifts are observed; for example, across the western boundary in the growth season from 1992 to 2009 consistent with the findings of Spreen et al. (2011). Ice fluxed across the northern boundary is thicker than across the western or eastern boundaries (Figure 4c) consistent with thicker, older ice entering the CB region from the Last Ice Area off northern Greenland (Petty et al., 2016; G. W. K. Moore et al., 2019). We point out the notable increases in ice entering and leaving the CB region during the 1995–2005 period in the growth season. This was explored by Kwok et al. (2013) and Petty et al. (2016), who attributed this with a strengthening of the anticyclonic gyre circulation (Proshutinsky et al., 2019). In general, the combination of thicker ice entering across the northern boundary and swifter ice velocities across the western boundary lead to advection into and out of the region being approximately equal (Figures 3c and 4a).

During the melt season, advective fluxes into and out of the CB are small and variable (Figure 4b). Smaller summertime ice advective fluxes can in part be attributed to slower wind speeds (and therefore slower ice drift) (Proshutinsky et al., 2002). Low convergence/divergence of ice in the melt season is associated with low sea-ice concentrations particularly in recent years (Figure 4f). Note that Howell et al. (2016) showed that July-October ice area fluxes exiting the basin across the western boundary were near-zero from 2008 to 2014 due to low SIC. It should be noted that mean ice thickness is comparable in each season (Figures 4c and 4d) since the melt/growth seasons cover the periods between the approximate thickest and thinnest ice and the mean is taken over the given season (Figure 1b).

Finally, we note that SIV advective fluxes across the eastern boundary (generally negative in the growth season) are small compared to fluxes across the northern and western boundaries, comprising approximately 6% of the net advective flux into or out of the CB region. Sea ice that crosses the eastern boundary is generally thinner (Figure 4), and drift speeds are slower compared to the other two boundaries (Figure S5 in Supporting Information S1).

Considering the general relationship between growth season SIV advection and melt season SIV changes, we find that larger ice export in the growth season is associated with larger SIV loss in the subsequent melt season (correlation coefficient $r = 0.66$). This complements the results of G. Moore et al. (2022), who found a similar correlation between winter SIV fluxes and June SIV anomalies in the region over the period 1980–2021. This is also consistent with the findings of D. G. Babb et al. (2019), who showed the 2015/2016 increase in wintertime ice export promoted early breakup of the ice pack and enhanced melt in the following summer. It also holds that smaller ice export into the region during the growth season is correlated with smaller SIV loss in the following melt season. For example, winds favoring sea-ice convergence in the 2016/2017 growth season were found to precondition the following summer for lower SIV losses (see D. Babb et al., 2020). In sum, increased (decreased) growth season ice export can precondition enhanced (reduced) SIV loss in the following melt season.

The trend in total SIV change is primarily influenced by thermodynamic changes within the CB (Figures 3c and 3d). Note that on average over 1979–2023 in the CB, we infer that thermodynamic processes contribute to approximately 80% (90%) percent of the total SIV change over a growth (melt) season. The linear trends in inferred thermodynamic SIV changes for the growth and melt seasons are almost equal in magnitude: $3.5 \pm 1.4 \times 10^{18}\ J\ \text{year}^{-1}$ (Figure 3c) and $-3.3 \pm 1.1 \times 10^{18}\ J\ \text{year}^{-1}$ (Figure 3d), respectively. These trends exist within the context of September SIV decreasing more rapidly than May SIV (Figure 1). A trend toward more ice growth in the growth season is consistent with May SIV losses not being as large as those in September. The nature of this will be further explored in subsequent sections when we discuss the other components of the atmosphere-ice-ocean heat budget.

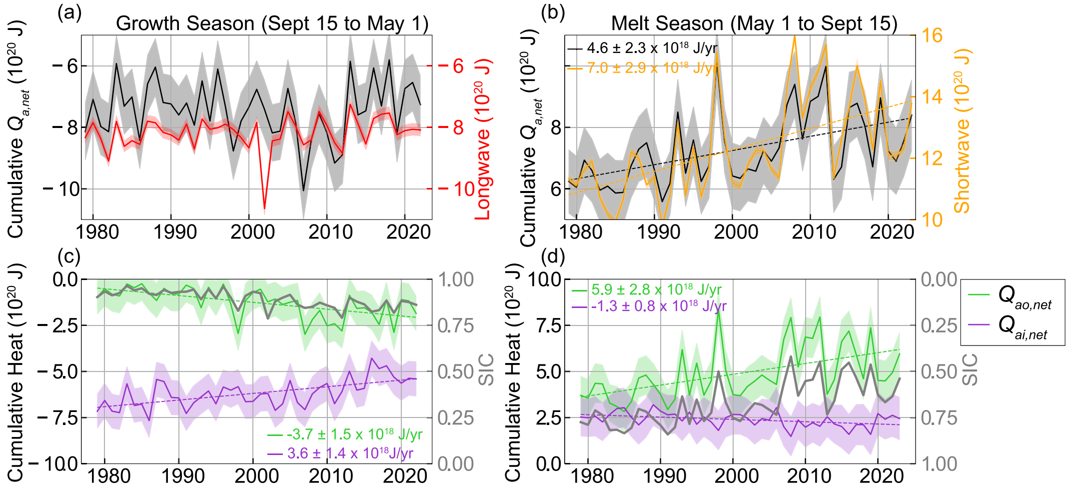

Figure 5. Timeseries of the net atmospheric heat input into the Canada Basin (CB) ice-ocean system [that is, cumulative sum of (2) and (3)] (gray), for the (a) growth, and (b) melt seasons. The cumulative longwave fluxes in growth seasons are shown in (a) [red] and the cumulative shortwave fluxes in melt seasons are shown in (b) [yellow]. Timeseries of the cumulative atmosphere-ice (purple) and cumulative atmosphere-ocean (green) heat input over the CB for the (c) growth, and (d) melt seasons; mean sea-ice concentration (SIC) from ERA5 for each season is also shown (gray) with the SIC axis inverted in panel (d). Positive values indicate input to the ice-ocean system from the atmosphere. Shading indicates uncertainty in ERA5 variables following Graham et al. (2019) and Renfrew et al. (2021). Linear trends with 95% confidence intervals are also shown. There are no statistically significant trends in panel (a). All the data are from ERA5 reanalysis.

3.2. Trends and Variability in Atmospheric Fluxes

Interannual changes in cumulative atmospheric heat input in any given season for 1979–2023 are related primarily to changes in SIC. For the growth season, there is no statistically significant interannual trend in $Q_{a,net}$ (i.e., the net cumulative atmospheric heat input to the surface ice-ocean system; Figure 5a). However, linear trends in net cumulative atmosphere-ice ($Q_{ai,net}$) and atmosphere-ocean ($Q_{ao,net}$) heat input are statistically significant ($3.6 \pm 1.4 \times 10^{18}$ J year^{-1} and $-3.7 \pm 1.5 \times 10^{18}$ J year^{-1}, respectively; Figure 5c). The negative linear trend in $Q_{ao,net}$ corresponds to an increase in heat release from the ocean to the atmosphere during the growth season, which results from increased open water area (e.g., a less consolidated winter ice pack and/or a more expansive marginal ice zone later into the growth season, etc.) and/or a warmer ocean. The positive trend in $Q_{ai,net}$ corresponds to less heat removal from the surface of the sea ice during the growth season, a manifestation of the trend to lower SIC. Overall, the opposing trends in $Q_{ai,net}$ and $Q_{ao,net}$ amount to no trend in $Q_{a,net}$ in the growth season (Figure 5a).

In the melt season, $Q_{a,net}$ has been increasing ($4.6 \pm 2.3 \times 10^{18}$ J year^{-1}) over the 1979–2023 period (Figure 5b). This increase is largely attributed to $Q_{ao,net}$, which has a linear trend of $5.9 \pm 2.8 \times 10^{18}$ J year^{-1} (Figure 5d) predominantly due to decreasing SIC (gray line, Figure 5d) allowing for more solar heating of the surface ocean (Figure 5b; a linear trend of $7.0 \pm 2.9 \times 10^{18}$ J year^{-1}). At the same time, there has been a decline in $Q_{ai,net}$ with a linear trend of $-1.3 \pm 0.8 \times 10^{18}$ J year^{-1} also attributed to the decline in SIC.

It is of note that incident downward shortwave radiation (Q_{SW}) in the melt season has a significant linear trend ($-4.2 \pm 1.3 \times 10^{18}$ J year^{-1}), while no other radiative flux exhibits statistically significant change from 1979 to 2023 (Figure S7 in Supporting Information S1). The trend in Q_{SW} to reduced insolation has been attributed to an increase in summertime low cloud cover (Huang et al., 2021) and limits solar input increases to the ice-ocean system (Figure 5b) by approximately 2.6×10^{18} J year^{-1}. This reduction is equivalent to about 0.5 m of sea-ice thickness over the CB from 1979 to 2023 (or approximately 1 cm per year).

So far, we have considered only net cumulative input over a melt or growth season. However, there is significant monthly variability in these values that provides important context for the growth/melt season trends. We explore this monthly variability next using the same variable names for net cumulative input but taken over any given month rather than season. In general, there is predominantly heat release from the ice-ocean system (i.e., $Q_{a,net} < 0$) from mid-September to the beginning of May and heat input (i.e., $Q_{a,net} > 0$) from May through mid-

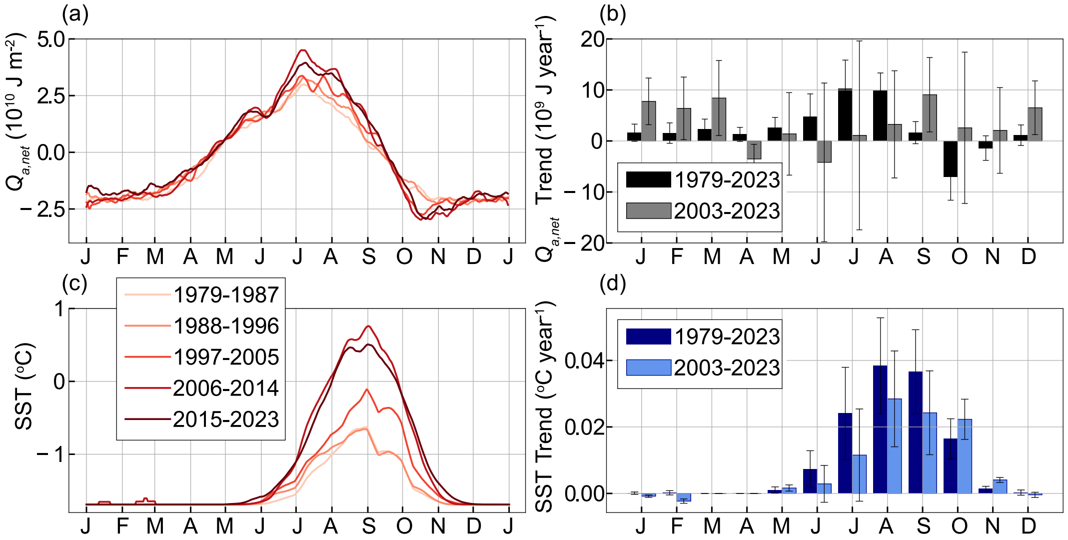

Figure 6. Interannual mean seasonal timeseries of (a) net atmospheric heat input to the ice-ocean system for a given month and (c) areal mean sea surface temperature (SST) over the Canada Basin (CB). Averages over the year groups shown in the legend are shown and a 10 day running mean is taken for each timeseries, (b) Monthly linear trends for the net monthly $Q_{a,net}$ for the CB with error bars indicating the 95% confidence interval for 1979–2023 (black) and 2003–2023 (gray), and (d) Same as (b) for areal mean SST for 1979–2023 (dark blue) and 2003–2023 (light blue). Data are from ERA5 reanalysis.

September (Figure 6a). Over the 1979 to 2023 period, there is a significant trend to more heat release in October from the ice-ocean system (-7×10^9 J year^{-1}; Figure 6b). By contrast, in each month from December through April, net cumulative monthly heat loss to the atmosphere from the ice and ocean has been decreasing (Figure 6b). Thus, over 1979–2023, a greater portion of heat release from the ice-ocean system occurs at the beginning of the growth season, particularly in October. Therefore, although there is no statistically significant trend in cumulative net growth season $Q_{a,net}$ (Figure 5a), there has been a shift in the seasonal distribution of heat release over 1979 through 2023 (Figures 6a and 6b). This shift in the seasonal distribution of heat release could result in a delay in fall freeze-up.

In all melt season months, May through September, there are significant positive linear trends in heat input to the system over 1979–2023 (Figure 6b) with the largest magnitude trends in July and August. These trends in heat input to the ice-ocean system are commensurate with the statistically significant trends in Figure 5b, which primarily result from the decreasing SIC.

As a precursor to our discussions of OHC in the next section, it is useful to examine atmospheric fluxes in context with sea-surface temperature (SST). SSTs have a seasonal cycle that peaks between July and September (Figures S2 in Supporting Information S1 and Figure 6c). In the CB, there has been statistically significant SST warming in the months of August to October over both the 1979–2023 period and over the recent two decades 2003–2023 (Figure 6d). Sea surface temperature increases in October (a month that sees a trend to more heat release from the system) highlight how relatively warm surface waters that persist into the beginning of the growth season lead to a greater proportion of heat loss from the ice-ocean system taking place at the start of the growth season. Throughout much of the remainder of the growth season in the recent two decades (December through March for 2003–2023), there are statistically significant increases in $Q_{a,net}$, indicating a significant decrease in heat release during these months (Figure 6b). These trends are generally due to a decrease in longwave, sensible, and, to a lesser extent, latent heat release in each month from December through March (Figure S8 in Supporting Information S1). Reduced longwave cooling, for example, could result from increased cloud cover; Letterly et al. (2016) noted increases over 1983–2013 in wintertime longwave downwelling due to increased cloud cover in the region.

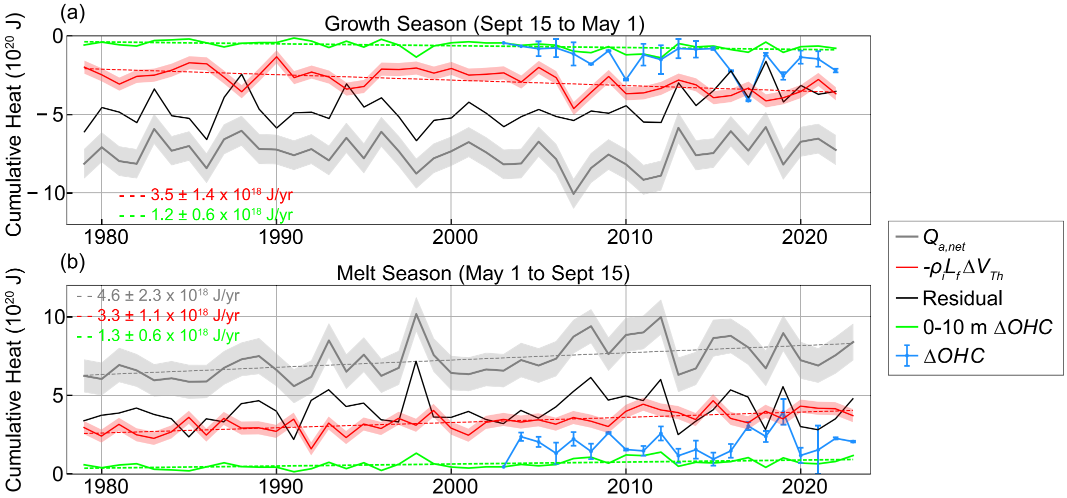

Figure 7. Net cumulative atmospheric heat input $Q_{a,net}$ (gray; Figure 5), the heat required for inferred thermodynamic sea-ice volume (SIV) change (red; Figure 3), the residual heat (black), ΔOHC for the surface layer (0–10 m; green) and ΔOHC for the entire upper water column (blue; error bars indicate one standard deviation) over the Canada Basin for the (a) growth and (b) melt seasons. Shading indicates uncertainty in Pan-Arctic Ice-Ocean Modeling and Assimilation System and ERA5 variables following Graham et al. (2019); Renfrew et al. (2021); Zhang and Rothrock (2003); Schweiger et al. (2011). Positive values indicate a flux into the ice-ocean system, or heat required to decrease SIV, or an increase in ocean heat content.

3.3. Ocean Heat Content and Residual Heat

Ocean observations (in situ and satellite-derived SST) are used here to construct a timeseries of OHC (Figure S9 in Supporting Information S1). Areal mean surface layer (i.e., top 10 m) OHC is of comparable magnitude to areal mean OHC between 10 and 30 m (Figure S9 in Supporting Information S1), where the NSTM is typically observed (Figure 2b). The deeper PSW layer (between 30 m and the depth of $S_A = 32.3$) contains around 90% of the OHC in the upper water column (Figure 2b and Figure S9b in Supporting Information S1). The seasonal change in OHC (ΔOHC) over each of the growth and melt seasons (Figure 7) is influenced by heat input/release to/from the ice-ocean system from the atmosphere, sea-ice melt/ablation or growth, lateral advection of different waters, and vertical fluxes between layers in the water column. We define a residual $Q_{a,net} - \rho_i L_f \Delta V_{th}$ to represent the heat added or removed from the ice-ocean system that is not used to change SIV. At least a fraction of this residual heat can be presumed to warm or cool (to the freezing temperature) the upper ocean, changing OHC.

In the growth season, the residual represents heat removed from the ice-ocean system that cools the upper ocean or sea ice. Heat removed from the system consistently exceeds the amount of heat loss required for the inferred ice growth; that is, the residual is negative (Figure 7a, black). In this season, ΔOHC is negative (i.e., the ocean is losing heat; Figure 7a) consistent with the negative residual. The increase in surface layer ΔOHC (at a rate of $1.2 \pm 0.6 \times 10^{18}$ J year^{-1} over the 1979–2023 period, Figure 7a, green) is consistent with the trend to warmer SSTs at the start of the growth season. We saw how this corresponds to increased $Q_{a,net}$ heat release in October (Figure 6b) but not when taken over the full growth season (Figure 7a, gray). We estimate that surface layer ΔOHC is on average 15% of the growth season residual, though this has increased from approximately 8% to up to 37% throughout the 1979–2023 period as the residual has been decreasing in magnitude (Figure 7a, green).

No statistically significant trends in ΔOHC for the upper water column are observed (Figure 7a, blue). We see interannual variations in the amount of heat extracted from the ice-ocean system (that does not result in sea-ice growth) accounted for by loss of ocean heat each growth season. In 2017, for example, the loss of ocean heat ΔOHC accounts for effectively the entirety of the residual, whereas in 2005, ΔOHC is a much smaller fraction of the residual (approximately 18%). Decreases in OHC during the growth season lead either to bottom ablation or inhibit the growth of sea ice (because the atmosphere must first cool the ocean to freezing temperature). Any trend to increased ocean heat loss in the growth season would be consistent with the findings of Zhong et al. (2022), who found that wintertime ocean-to-ice heat fluxes had more than doubled from 2006–2012 to 2013–2018 predominantly driven by the entrainment of subsurface heat. Nevertheless, on average only about 40% of the residual is accounted for by ΔOHC in the growth season over the 2003–2023 period.

In the melt season, the residual represents additional heat put into the ice-ocean system (i.e., net positive $Q_{a,net}$) compared to the heat required for inferred ice melt. In general, there is much more heat added to the system than is used to melt ice (black line, Figure 7b). This corresponds to a positive ΔOHC (Figure 7b). The amount of heat estimated to warm the surface layer is only a small fraction of the melt season residual (7%–24% of residual; Figure 7b, green), though the seasonal change in OHC in the surface ocean is increasing over the 1979–2023 period (with a linear trend of $1.3 \pm 0.6 \times 10^{18}\ J\ \text{year}^{-1}$) and is consistent with monthly trends in SSTs (Figure 6d). ΔOHC for the upper water column accounts for 34% of the residual on average (Figure 7b, blue) with high variability and no statistically significant trends. This leaves a large portion of the melt season residual unaccounted for.

Data limitations prevent us from tracking all of the heat in the system and closing the budget. Ocean observations are sparse in any given year, particularly at the margins of the CB where ocean heat gains and losses can be strong and localized, tightly coupled to seasonal boundary currents and maximum sea-ice variability and change. Furthermore, there are seasonal and interannual lags in the system such that heat flux residuals in 1 year may not necessarily relate to OHC change in that same year. For example, warm surface waters in the Chukchi Sea in one summer may take years to ventilate the PSW layer in the interior CB (Timmermans et al., 2018). Nevertheless, in the next section, we speculate on possible sinks for the residual heat estimated here.

4. Summary and Discussion

Since the mid-2000s, the CB region has seen significant MYI loss. By partitioning seasonal sea-ice volume changes into advective and thermodynamic components, we have shown that trends in seasonal SIV changes in the CB over 1979–2023 are dominated by thermodynamics as opposed to advective convergences and divergences. This result agrees with Proshutinsky et al. (2019), who found that from 2003 to 2018 seasonal changes in sea ice in the region were primarily driven by local ice thermodynamics. Our results indicate increases in both inferred melt and growth. The more rapid rate of SIV loss in September compared to May is such that the rate of increase over 1979–2023 in inferred growth in the growth season is nearly equal to the rate of increase of inferred sea-ice melt in the melt season. At the same time, there has been an interannual increase in heat input to the ice-ocean system during the melt season with the largest increases taking place in July and August; this is a manifestation of the ice-albedo feedback (e.g., Perovich et al., 2008; D. G. Babb et al., 2019). By contrast, we find no interannual change in net heat removal during the growth season. The inferred interannual increases in wintertime growth are consistent with an ice-growth feedback in the face of thinner ice requiring less heat to grow by conduction at the same rate as thicker ice (Bitz & Roe, 2004; Maykut, 1986); for example, growing 1 m thick ice by 5 cm requires approximately two times more heat release compared to growing 0.5 m of ice by 5 cm.

Our results are broadly consistent with the findings of Ricker et al. (2021), who analyzed model data from North Atlantic/Arctic Ocean–Sea Ice Model and PIOMAS, to deduce a negative feedback where thin ice grows faster in some Arctic marginal seas (including the Beaufort Sea). In addition, Rheinlænder et al. (2024) found that from 2000 through 2018 in the CB region, there was an increase in the occurrence of wintertime leads, giving rise to enhanced ice drift, which results in more open water area where there is faster growth of new ice. It is important to note that the level of uncertainty in our conclusions depends on the extent to which PIOMAS can accurately represent both thermodynamic and dynamic sea-ice processes. For example, PIOMAS relies on parameterizations for lead formation and ridging, and the model has relatively coarse lateral resolution relative to the scales of these features. As such, the more frequent occurrence of wintertime leads (e.g., Lewis & Hutchings, 2019; Rheinlænder et al., 2022; Rheinlænder et al., 2024) may not be well represented and could lead to an underestimation of the dynamical SIV changes in our analysis. Further to this, Zhang (2021) showed the thinner Arctic ice pack deforms more easily, leading to more frequent periods of open water, which ultimately enhances ice growth. By contrast, Petty et al. (2018) asserted that the negative feedback associated with thickness-dependent growth rates becomes less significant as the mean October ice state declines to near ice-free conditions. Our results show a significant increase in October atmospheric heat release that acts to counterbalance increased melt season atmospheric heating.

Under continued warming, the general expectation may be that wintertime ice growth will slow with a tendency to increased losses of *OHC* throughout the growth season (e.g., Cornish et al., 2022). For example, Zhong et al. (2022) showed enhanced decreases in *OHC* throughout the growth season in the most recent decade, which could suppress any negative ice-growth feedback. However, *OHC* is the least constrained component of the atmosphere-ice-ocean heat budget; the largest ocean heat reservoir is below the mixed layer and therefore must be quantified by in situ measurements, which have major spatial and temporal gaps.

Although the quantification of OHC is poorly constrained, our results show that approximately one-third of the difference between net atmospheric heat input and heat required for thermodynamic changes in SIV (i.e., the residual) may be accounted for via warming and cooling of the upper water column in either season. The remainder of the growth season residual could be due to the additional heat required to grow ice when snow is present to act as an insulator. For example, (Lim et al., 2022) found that a 13–18 cm thick snow layer could inhibit ice growth by approximately 10 cm throughout a winter. The heat equivalent of this over the CB region could account for around 8% of the mean winter residual. Unaccounted residual heat in the melt season could be due to the melting of a snow layer (e.g., again taking a 13–18 cm thick snow layer, we estimate its melt could account for approximately 3% of the residual heat). Further, melt ponds may play a role with increased heat absorption in the presence of melt ponds potentially amounting up to 59% of the residual based on melt pond area and albedo estimates of Fetterer and Untersteiner (1998); Perovich and Polashenski (2012). The potential contribution of melt ponds to the residual could be at least partly addressed with a seasonally varying sea-ice albedo (see Perovich et al., 2011). Accounting for a seasonally varying sea-ice albedo could have a notable influence on our results. For example, taking an ice albedo of 0.6 (only 16% smaller than the value of 0.7 used here) yields a 16% increase in solar absorption in the melt season, which amounts to approximately one-third of our previously estimated residual. The additional complexity of seasonally variable ice albedo and its influence on this atmosphere-ice-ocean heat budget is an important area for future research. Additionally, measurements of the ocean-ice-snow system should be the focus of future work and may shed crucial light on the evolution and future state of sea ice in the CB.

Data Availability Statement

Sea-ice velocity, effective thickness, and concentration are from the PIOMAS and are available at https://pscfiles.apl.uw.edu/zhang/PIOMAS/data/v2.1/ (Zhang & Rothrock, 2003). Atmospheric heat and radiative fluxes as well as SIC and SST are from the ECMWF reanalysis data product (ERA5) and are available from the Copernicus Climate Data Store at https://doi.org/10.24381/cds.adbb2d47 (Hersbach et al., 2018). Sea surface salinity reanalysis is from the ECMWF Ocean Reanalysis System 5 (ORAS5) and is available at https://doi.org/10.24381/cds.67e8eeb7. The ITP data were collected and made available by the ITP Program (Toole et al., 2011; R. Krishfield et al., 2008) based at the Woods Hole Oceanographic Institution (https://www2.whoi.edu/site/itp/) and are available at https://doi.org/10.7289/v5mw2f7x. Conductivity, Temperature, and Depth data were collected and made available by the NSF Beaufort Gyre Observing Sytem (BGOS) (https://www2.whoi.edu/site/beaufortgyre/) in collaboration with researchers from Fisheries and Oceans Canada at the Institute of Ocean Sciences (IOS). Ice-Tethered Profiler and CTD data are also available at the NSF Arctic Data Center (https://arcticdata.io/).

Acknowledgments
Funding was provided by the National Science Foundation, Division of Polar Programs under Grant 1950077, and the Office of Naval Research (ONR) Multidisciplinary University Research Initiatives Program (N00014-23-1-2014).

References

Arroyo, A., Timmermans, M.-L., Le Bras, I., Williams, W., & Zimmermann, S. (2023). Declining O2 in the Canada Basin halocline consistent with physical and biogeochemical effects of Pacific Summer Water warming. *Journal of Geophysical Research: Oceans*, *128*(4), e2022JC019418. https://doi.org/10.1029/2022jc019418

Babb, D., Landy, J., Lukovich, J., Haas, C., Hendricks, S., Barber, D., & Galley, R. (2020). The 2017 reversal of the Beaufort Gyre: Can dynamic thickening of a seasonal ice cover during a reversal limit summer ice melt in the Beaufort Sea? *Journal of Geophysical Research: Oceans*, *125*(12), e2020JC016796. https://doi.org/10.1029/2020jc016796

Babb, D. G., Galley, R. J., Howell, S. E., Landy, J. C., Stroeve, J. C., & Barber, D. G. (2022). Increasing multiyear sea ice loss in the Beaufort sea: A new export pathway for the diminishing multiyear ice cover of the Arctic Ocean. *Geophysical Research Letters*, *49*(9), e2021GL097595. https://doi.org/10.1029/2021gl097595

Babb, D. G., Landy, J., Barber, D., & Galley, R. (2019). Winter sea ice export from the Beaufort sea as a preconditioning mechanism for enhanced summer melt: A case study of 2016. *Journal of Geophysical Research: Oceans*, *124*(9), 6575–6600. https://doi.org/10.1029/2019jc015053

Batrak, Y., & Müller, M. (2019). On the warm bias in atmospheric reanalyses induced by the missing snow over Arctic sea-ice. *Nature Communications*, *10*(1), 4170. https://doi.org/10.1038/s41467-019-11975-3

Bitz, C. M., & Roe, G. (2004). A mechanism for the high rate of sea ice thinning in the Arctic ocean. *Journal of Climate*, *17*(18), 3623–3632. https://doi.org/10.1175/1520-0442(2004)017<3623:amfthr>2.0.co;2

Brucker, L., Cavalieri, D. J., Markus, T., & Ivanoff, A. (2014). Nasa Team 2 sea ice concentration algorithm retrieval uncertainty. *IEEE Transactions on Geoscience and Remote Sensing*, *52*(11), 7336–7352. https://doi.org/10.1109/tgrs.2014.2311376

Cornish, S. B., Johnson, H. L., Mallett, R. D. C., Dörr, J., Kostov, Y., & Richards, A. E. (2022). Rise and fall of sea ice production in the Arctic Ocean's ice factories. *Nature Communications*, *13*(1), 7800. Retrieved 2024-12-26, from. https://doi.org/10.1038/s41467-022-34785-6

Fetterer, F., & Untersteiner, N. (1998). Observations of melt ponds on Arctic sea ice. *Journal of Geophysical Research*, *103*(C11), 24821–24835. https://doi.org/10.1029/98jc02034

Graham, R. M., Cohen, L., Ritzhaupt, N., Segger, B., Graversen, R. G., Rinke, A., et al. (2019). Evaluation of six atmospheric reanalyses over Arctic sea ice from winter to early summer. *Journal of Climate*, *32*(14), 4121–4143. https://doi.org/10.1175/jcli-d-18-0643.1

Hall, S. B., Subrahmanyam, B., & Morison, J. H. (2021). Intercomparison of salinity products in the Beaufort gyre and Arctic Ocean. *Remote Sensing*, *14*(1), 71. https://doi.org/10.3390/rs14010071

Herrmannsdörfer, L., Müller, M., Shupe, M. D., & Rostosky, P. (2023). Surface temperature comparison of the Arctic winter MOSAiC observations, ERA5 reanalysis, and MODIS satellite retrieval. *Element Science Anth*, *11*(1), 00085. https://doi.org/10.1525/elementa.2022.00085

Hersbach, H., Bell, B., Berrisford, P., Biavati, G., Horányi, A., Muñoz Sabater, J., et al. (2018). ERA5 hourly data on single levels from 1979 to present. *Copernicus Climate Change Service (C3S) Climate Data Store (CDS)*, 10.

Howell, S. E., Brady, M., Derksen, C., & Kelly, R. E. (2016). Recent changes in sea ice area flux through the Beaufort Sea during the summer. *Journal of Geophysical Research: Oceans*, *121*(4), 2659–2672. https://doi.org/10.1002/2015jc011464

Huang, Y., Ding, Q., Dong, X., Xi, B., & Baxter, I. (2021). Summertime low clouds mediate the impact of the large-scale circulation on Arctic sea ice. *Communications Earth and Environment*, *2*(1), 38. https://doi.org/10.1038/s43247-021-00114-w

Hutchings, J., & Rigor, I. (2012). Role of ice dynamics in anomalous ice conditions in the Beaufort Sea during 2006 and 2007. *Journal of Geophysical Research*, *117*(C8). https://doi.org/10.1029/2011jc007182

Jackson, J. M., Carmack, E., McLaughlin, F., Allen, S. E., & Ingram, R. (2010). Identification, characterization, and change of the near-surface temperature maximum in the Canada Basin, 1993–2008. *Journal of Geophysical Research*, *115*(C5). https://doi.org/10.1029/2009jc005265

Kalnay, E., Kanamitsu, M., Kistler, R., Collins, W., Deaven, D., Gandin, L., et al. (1996). The NCEP/NCAR 40-year reanalysis project. *Bulletin America Meteorology Social*, *77*(3), 437–471. https://doi.org/10.1175/1520-0477(1996)077<0437:tnyrp>2.0.co;2

Kong, B., Liu, N., Fan, L., Lin, L., Yang, L., Chen, H., et al. (2022). Evaluation of surface meteorology parameters and heat fluxes from CFSR and ERA5 over the Pacific Arctic Region. *Quarterly Journal of the Royal Meteorological Society*, *148*(747), 2973–2990. https://doi.org/10.1002/qj.4346

Krishfield, R., Toole, J., Proshutinsky, A., & Timmermans, M.-L. (2008). Automated ice-tethered profilers for seawater observations under pack ice in all seasons. *Journal of Atmospheric and Oceanic Technology*, *25*(11), 2091–2105. https://doi.org/10.1175/2008jtecho587.1

Krishfield, R. A., Proshutinsky, A., Tateyama, K., Williams, W. J., Carmack, E. C., McLaughlin, F. A., & Timmermans, M.-L. (2014). Deterioration of perennial sea ice in the Beaufort Gyre from 2003 to 2012 and its impact on the oceanic freshwater cycle. *Journal of Geophysical Research: Oceans*, *119*(2), 1271–1305. https://doi.org/10.1002/2013jc008999

Kwok, R. (2018). Arctic sea ice thickness, volume, and multiyear ice coverage: Losses and coupled variability (1958–2018). *Environmental Research Letters*, *13*(10), 105005. https://doi.org/10.1088/1748-9326/aae3ec

Kwok, R., Spreen, G., & Pang, S. (2013). Arctic sea ice circulation and drift speed: Decadal trends and ocean currents. *Journal of Geophysical Research: Oceans*, *118*(5), 2408–2425. Retrieved 2024-10-08, from. https://doi.org/10.1002/jgrc.20191

Letterly, A., Key, J., & Liu, Y. (2016). The influence of winter cloud on summer sea ice in the Arctic, 1983–2013. *Journal of Geophysical Research: Atmospheres*, *121*(5), 2178–2187. Retrieved 2025-01-06, from. https://doi.org/10.1002/2015JD024316

Lewis, B. J., & Hutchings, J. K. (2019). Leads and associated Sea Ice drift in the Beaufort Sea in winter. *Journal of Geophysical Research: Oceans*, *124*(5), 3411–3427. Retrieved 2024-12-26, from. https://doi.org/10.1029/2018JC014898

Lim, W.-I., Park, H.-S., Stewart, A. L., & Seo, K.-H. (2022). Suppression of Arctic sea ice growth in the Eurasian–Pacific seas by winter clouds and snowfall. *Journal of Climate*, *35*(2), 669–686. https://doi.org/10.1175/jcli-d-21-0282.1

Maslanik, J., Stroeve, J., Fowler, C., & Emery, W. (2011). Distribution and trends in Arctic sea ice age through spring 2011. *Geophysical Research Letters*, *38*(13). Retrieved 2024-10-14, from. https://doi.org/10.1029/2011GL047735

Maslanik, J. A., Serreze, M. C., & Agnew, T. (1999). On the record reduction in 1998 western Arctic sea-ice cover. *Geophysical Research Letters*, *26*(13), 1905–1908. https://doi.org/10.1029/1999gl900426

Maykut, G. A. (1986). The surface heat and mass balance. In *The geophysics of sea ice* (pp. 395–463). Springer.

Melling, H., Johnston, P. H., & Riedel, D. A. (1995). Measurements of the underside topography of sea ice by moored subsea sonar. *Journal of Atmospheric and Oceanic Technology*, *12*(3), 589–602. https://doi.org/10.1175/1520-0426(1995)012<0589:motuto>2.0.co;2

Mogensen, K., Balmaseda, M. A., & Weaver, A. (2012). The NEMOVAR ocean data assimilation system as implemented in the ECMWF ocean analysis for system 4.

Moore, G., Steele, M., Schweiger, A. J., Zhang, J., & Laidre, K. L. (2022). Thick and old sea ice in the Beaufort Sea during summer 2020/21 was associated with enhanced transport. *Communications Earth and Environment*, *3*(1), 198. https://doi.org/10.1038/s43247-022-00530-6

Moore, G. W. K., Schweiger, A., Zhang, J., & Steele, M. (2019). Spatiotemporal variability of Sea Ice in the Arctic's Last ice area. *Geophysical Research Letters*, *46*(20), 11237–11243. Retrieved 2024-10-07, from. https://doi.org/10.1029/2019GL083722

Pegau, W. S., & Paulson, C. A. (2001). The albedo of Arctic leads in summer. *Annals of Glaciology*, *33*, 221–224. https://doi.org/10.3189/172756401781818833

Peralta-Ferriz, C., & Woodgate, R. A. (2015). Seasonal and interannual variability of pan-Arctic surface mixed layer properties from 1979 to 2012 from hydrographic data, and the dominance of stratification for multiyear mixed layer depth shoaling. *Progress in Oceanography*, *134*, 19–53. https://doi.org/10.1016/j.pocean.2014.12.005

Perovich, D. K., Light, B., Eicken, H., Jones, K. F., Runciman, K., & Nghiem, S. V. (2007). Increasing solar heating of the Arctic Ocean and adjacent seas, 1979–2005: Attribution and role in the ice-albedo feedback. *Geophysical Research Letters*, *34*(19). https://doi.org/10.1029/2007gl031480

Perovich, D. K., Nghiem, S. V., Markus, T., & Schweiger, A. (2007). Seasonal evolution and interannual variability of the local solar energy absorbed by the Arctic sea ice–ocean system. *Journal of Geophysical Research*, *112*(C3). https://doi.org/10.1029/2006jc003558

Perovich, D. K., & Polashenski, C. (2012). Albedo evolution of seasonal Arctic sea ice. *Geophysical Research Letters*, *39*(8). https://doi.org/10.1029/2012gl051432

Perovich, D. K., Richter-Menge, J. A., Jones, K. F., & Light, B. (2008). Sunlight, water, and ice: Extreme Arctic sea ice melt during the summer of 2007. *Geophysical Research Letters*, *35*(11). https://doi.org/10.1029/2008gl034007

Perovich, D. K., Richter-Menge, J. A., Jones, K. F., Light, B., Elder, B. C., Polashenski, C., et al. (2011). Arctic sea-ice melt in 2008 and the role of solar heating. *Annals of Glaciology*, *52*(57), 355–359. https://doi.org/10.3189/172756411795931714

Petty, A. A., Holland, M. M., Bailey, D. A., & Kurtz, N. T. (2018). Warm Arctic, increased winter sea ice growth? *Geophysical Research Letters*, *45*(23), 12–922. https://doi.org/10.1029/2018gl079223

Petty, A. A., Hutchings, J. K., Richter-Menge, J. A., & Tschudi, M. A. (2016). Sea ice circulation around the Beaufort Gyre: The changing role of wind forcing and the sea ice state. *Journal of Geophysical Research: Oceans*, *121*(5), 3278–3296. Retrieved 2024-10-07, from. https://doi.org/10.1002/2015JC010903

Proshutinsky, A., Bourke, R. H., & McLaughlin, F. A. (2002). The role of the Beaufort Gyre in Arctic climate variability: Seasonal to decadal climate scales. *Geophysical Research Letters*, *29*(23). Retrieved 2024-10-08, from. https://doi.org/10.1029/2002GL015847

Proshutinsky, A., Krishfield, R., Toole, J., Timmermans, M.-L., Williams, W., Zimmermann, S., et al. (2019). Analysis of the Beaufort Gyre freshwater content in 2003–2018. *Journal of Geophysical Research: Oceans*, *124*(12), 9658–9689. https://doi.org/10.1029/2019jc015281

Renfrew, I. A., Barrell, C., Elvidge, A., Brooke, J., Duscha, C., King, J., et al. (2021). An evaluation of surface meteorology and fluxes over the Iceland and Greenland Seas in ERA5 reanalysis: The impact of sea ice distribution. *Quarterly Journal of the Royal Meteorological Society*, *147*(734), 691–712. https://doi.org/10.1002/qj.3941

Rheinlænder, J. W., Davy, R., Ólason, E., Rampal, P., Spensberger, C., Williams, T. D., et al. (2022). Driving mechanisms of an extreme winter Sea Ice breakup event in the Beaufort sea. *Geophysical Research Letters*, *49*(12), e2022GL099024. Retrieved 2025-01-07, from. https://doi.org/10.1029/2022GL099024

Rheinlænder, J. W., Regan, H., Rampal, P., Boutin, G., Olason, E., & Davy, R. (2024). Breaking the ice: Exploring the changing dynamics of winter breakup events in the Beaufort Sea. *Journal of Geophysical Research: Oceans*, *129*(4), e2023JC020395. https://doi.org/10.1029/2023jc020395

Ricker, R., Kauker, F., Schweiger, A., Hendricks, S., Zhang, J., & Paul, S. (2021). Evidence for an increasing role of ocean heat in Arctic winter sea ice growth. *Journal of Climate*, *34*(13), 5215–5227. https://doi.org/10.1175/jcli-d-20-0848.1

Schweiger, A., Lindsay, R., Zhang, J., Steele, M., Stern, H., & Kwok, R. (2011). Uncertainty in modeled Arctic sea ice volume. *Journal of Geophysical Research*, *116*(C8), C00D06. https://doi.org/10.1029/2011jc007084

Seo, M., Kim, H.-C., Lee, K.-S., Seong, N.-H., Lee, E., Kim, J., & Han, K.-S. (2020). Characteristics of the reanalysis and satellite-based surface net radiation data in the Arctic. *Journal of Sensors*, *2020*, 1–13. https://doi.org/10.1155/2020/8825870

Spreen, G., Kwok, R., & Menemenlis, D. (2011). Trends in Arctic sea ice drift and role of wind forcing: 1992-2009. *Geophysical Research Letters*, *38*(19). n/a–n/a. Retrieved 2025-01-06, from. https://doi.org/10.1029/2011GL048970

Thorndike, A., & Colony, R. (1982). Sea ice motion in response to geostrophic winds. *Journal of Geophysical Research*, *87*(C8), 5845–5852. https://doi.org/10.1029/jc087ic08p05845

Timmermans, M.-L. (2015). The impact of stored solar heat on Arctic sea ice growth. *Geophysical Research Letters*, *42*(15), 6399–6406. https://doi.org/10.1002/2015gl064541

Timmermans, M.-L., Toole, J., & Krishfield, R. (2018). Warming of the interior Arctic Ocean linked to sea ice losses at the basin margins. *Science Advances*, *4*(8), eaat6773. https://doi.org/10.1126/sciadv.aat6773

Timmermans, M.-L., & Toole, J. M. (2023). The Arctic Ocean's Beaufort Gyre. *Annual Review of Marine Science*, *15*(1), 223–248. https://doi.org/10.1146/annurev-marine-032122-012034

Toole, J. M., Krishfield, R. A., Timmermans, M.-L., & Proshutinsky, A. (2011). The ice-tethered profiler: Argo of the Arctic. *Oceanography*, *24*(3), 126–135. https://doi.org/10.5670/oceanog.2011.64

Toole, J. M., Timmermans, M.-L., Perovich, D. K., Krishfield, R. A., Proshutinsky, A., & Richter-Menge, J. A. (2010). Influences of the ocean surface mixed layer and thermohaline stratification on Arctic Sea ice in the central Canada Basin. *Journal of Geophysical Research*, *115*(C10). https://doi.org/10.1029/2009jc005660

Wang, C., Graham, R. M., Wang, K., Gerland, S., & Granskog, M. A. (2019). Comparison of ERA5 and ERA-Interim near-surface air temperature, snowfall and precipitation over Arctic sea ice: Effects on sea ice thermodynamics and evolution. *The Cryosphere*, *13*(6), 1661–1679. https://doi.org/10.5194/tc-13-1661-2019

Wang, X., Key, J., Kwok, R., & Zhang, J. (2016). Comparison of Arctic sea ice thickness from satellites, aircraft, and PIOMAS data. *Remote Sensing*, *8*(9), 713. https://doi.org/10.3390/rs8090713

Woodgate, R. A., Weingartner, T., & Lindsay, R. (2010). The 2007 Bering Strait oceanic heat flux and anomalous Arctic sea-ice retreat. *Geophysical Research Letters*, *37*(1). https://doi.org/10.1029/2009gl041621

Zhang, J. (2021). Recent slowdown in the decline of Arctic sea ice volume under increasingly warm atmospheric and oceanic conditions. *Geophysical Research Letters*, *48*(18), e2021GL094780. https://doi.org/10.1029/2021gl094780

Zhang, J., Lindsay, R., Schweiger, A., & Steele, M. (2013). The impact of an intense summer cyclone on 2012 Arctic sea ice retreat. *Geophysical Research Letters*, *40*(4), 720–726. https://doi.org/10.1002/grl.50190

Zhang, J., & Rothrock, D. A. (2003). Modeling global sea ice with a thickness and enthalpy distribution model in generalized curvilinear coordinates. *Monthly Weather Review*, *131*(5), 845–861. https://doi.org/10.1175/1520-0493(2003)131<0845:mgsiwa>2.0.co;2

Zhong, W., Cole, S. T., Zhang, J., Lei, R., & Steele, M. (2022). Increasing winter ocean-to-ice heat flux in the Beaufort Gyre region, Arctic Ocean over 2006–2018. *Geophysical Research Letters*, *49*(2), e2021GL096216. https://doi.org/10.1029/2021gl096216